The Astrophysical Journal, 927:143 (15pp), 2022 March 10 https://doi.org/10.3847/1538-4357/ac496f

The Evolution of the Orbital Lightcurve of Hercules X-1 with 35 Day Phase

Yuyang Wang and Denis Leahy
Department of Physics & Astronomy, University of Calgary, Calgary, Alberta, T2N 1N4 Canada; leahy@ucalgary.ca
Received 2021 December 5; revised 2022 January 6; accepted 2022 January 7; published 2022 March 10

Abstract

Hercules X-1/HZ Hercules (Her X-1/HZ Her) is an X-ray binary monitored by multiple X-ray missions since the last century. With the abundance of long-term observations, we present a complete set of orbital lightcurves of Her X-1/HZ Her during the six states of the 35 day cycle in multiple energy bands. These illustrate in detail the changing lightcurve caused by the rotating twisted-tilted accretion disk surrounding the neutron star. The orbital lightcurves during the main high state are analyzed in 0.05 35 day phase intervals. These show the regular occurrence of pre-eclipse dips that march to earlier orbital phases as the 35 day phases increase. From the multiband lightcurves, we derive the time-average orbital phase dependence of column density for photoelectric absorption and energy-independent transmission as a function of 35 day phase. The X-ray lightcurves during low states are similar in shape to the optical low-state lightcurve, but X-ray leads optical by $\simeq$0.04–0.08 in orbital phase.

Unified Astronomy Thesaurus concepts: X-ray binary stars (1811); Light curves (918); Accretion (14); Neutron stars (1108)

1. Introduction

Hercules X-1/HZ Hercules (Her X-1/HZ Her) is an X-ray binary of constant research interest for its abundant observational phenomena. The X-ray emission of the system features three timescales—the 1.24 s pulsation of Her X-1, the 1.7 day binary period, and the super-orbital 35 day cycle. The counter-precession of a twisted-tilted accretion disk is believed to be the reason causing the 35 day cycle (Petterson 1975; Gerend & Boynton 1976; Scott & Leahy 1999; Scott et al. 2000; Leahy 2002).

Since its discovery in 1971 as an X-ray source, Her X-1 has been observed by various missions, accumulating large amounts of data. The binary system has multiwavelength emissions, including optical, ultraviolet (UV), extreme ultraviolet (EUV), and X-ray. UV and EUV radiation comes from the inner disk and the irradiated surface of HZ Her (Leahy et al. 2000, 2020), and is modeled by Leahy (2003). Optical emissions mainly originate from the X-ray heating of the companion star HZ Her by Her X-1. The modulations of the optical lightcurves of the 1.7 day orbits have been studied and give support to the precessing accretion disk model (Deeter et al. 1976; Gerend & Boynton 1976; Jurua et al. 2011). In contrast, a recent study (Kolesnikov et al. 2020) models the optical lightcurves using a precessing neutron star and a forced disk.

Previous studies of the X-ray observations have shown the properties of the 35 day cycle and pulse profile in detail. The long-term properties of the 35 day cycle of Her X-1 were studied using RXTE/ASM (Leahy & Igna 2011) and Swift/BAT (Leahy & Wang 2020) observations. The twisted-tilted counter-precessing disk model (Petterson 1975) has been developed to describe 35 day lightcurve behaviors in multiple wavelengths (Leahy 2002). The X-ray pulsations during the main high (MH) state were modeled with an accretion column by Leahy (2004). Scott et al. (2000) modeled the evolution of the pulse profile of Her X-1 with the 35 day cycle, which was explained by the systematic changes in obscuration by the inner and outer disk edges. An alternative explanation for the change of the pulse shape with the 35 day phase is the free precession of the neutron star (Postnov et al. 2013).

Investigations of the timescale of the 1.7 day binary period focus on the properties of the eclipse, including ingress and egress, as well as dips, which are rapid drops in X-ray flux.

The eclipse egress of Her X-1/HZ Her is rapid and less varying compared to the ingress. Oegelman & Truemper (1988) show in their Figure B1 the egress lightcurves of several orbits observed by EXOSAT in 1984 and 1985. They found an increasing amount of absorbing material with the 35 day phase, which is caused by the changes in the X-ray illumination of the atmosphere of HZ Her, or possibly by an extended structure of the outer edge of the accretion disk. Leahy (1995) studied five eclipses from GINGA/LAC observations between 1988 and 1989. Their spectra analysis indicates that during MH and the early short high (SH) state, most of the radiation from the neutron star is scattered without being absorbed, while in the late high states, absorption dominates. Leahy & Yoshida (1995) extracted the structure of the atmosphere and wind around HZ Her by analyzing an X-ray ingress and eclipse during the high state, observed with the GINGA satellite in 1989. Leahy & Abdallah (2014) analyzed eight ingress and egress segments of high-resolution lightcurves to measure the radius and evolutionary state of HZ Her. Leahy (2015) modeled the X-ray corona from electron scattering during high-state X-ray eclipses.

The existence of dips, and the fact that pre-eclipse dips march to earlier orbital phases, have been known since the very first observations of the system (Giacconi et al. 1973; Gorecki et al. 1982). Previous studies of the dips of Her X-1 include Reynolds & Parmar (1995) with EXOSAT data, Igna & Leahy (2011) with RXTE/PCA observations, Shakura et al. (1999) and Igna & Leahy (2012) in theory, and, statistically, Leahy & Igna (2011).

From the X-ray spectrum during the dips, the dips are caused by absorbing material containing nearly neutral iron, thus are nearly nonionized (cold). Based on 44 sections of GINGA/LAC data from 1988 through 1990, Leahy (1997) found that the dip column density increases with orbital phase, but not with the 35 day phase. They also found that there is no strong correlation between the duration of the absorption dips and the orbital or 35 day phases. Recent studies on Her X-1 have made use of the RXTE/PCA data. The fraction of time in the dip was found to vary with orbital phase, as well as the 35 day phase (Leahy & Igna 2011).

However, the number of binary orbits investigated in these studies is relatively small. Oftentimes, only part of the orbital cycle is explored. On the other hand, X-ray monitors produce long-term observations of the system with significantly more orbital cycles but lower time resolution and sensitivity. As a result, the monitoring data were analyzed with an emphasis on the super-orbital 35 day cycle. There exist no comprehensive analyses of the orbital lightcurve of Her X-1/HZ Her in X-ray to date. In this paper, we present the time-average orbital lightcurves derived from more than ten years of observations in multiple X-ray energy bands. We determine the changes of the orbital lightcurves with the 35 day phase. Further investigation of the pre-eclipse absorption dips is carried out during MH.

In Section 2, the X-ray observations are described. Section 3 describes the methods employed to create and fit the orbital lightcurves. Section 4 presents the results for the orbital lightcurves during all six states of the 35 day cycle. Section 5 discusses the evolution of the orbital lightcurve with the 35 day phase and the physical implications. Section 6 summarizes and concludes the paper.

2. Observations

2.1. Swift/BAT

The Burst Alert Telescope (BAT) on board the Neil Gehrels Swift Observatory is an X-ray monitoring instrument, from which long-term lightcurves are created (Krimm et al. 2013). The data are available at the website,[1] from which we downloaded the 15–50 keV lightcurve of Her X-1. 71,165 points were included, covering 14 yr of observations from 2005 February to 2019 November. Exposure times per point range from 64 to 2672 s. Times were recorded as mission times in units of seconds, and were converted to MJD before further analysis.

2.2. RXTE/ASM

The Rossi X-Ray Timing Explorer (RXTE) All-Sky Monitor (ASM) monitored the sky in the soft energy band of 2–12 keV with exposure times of approximately 90 minutes (Levine et al. 1996). The Her X-1 lightcurve is available at the Massachusetts Institute of Technology RXTE project online database.[2] The RXTE/ASM data cover the time period from 1996 January to 2011 December, with a total number of 95,782 points.

2.3. MAXI

The Monitor of All-sky X-ray Image (MAXI) on the International Space Station monitors Her X-1 in the energy band of 2–20 keV (Matsuoka et al. 2009). Simultaneous observations in three narrower bands are available for Her X-1: 2–4 keV (labeled as "Band 1" in this paper), 4–10 keV ("Band 2"), and 10–20 keV ("Band 3").

For MAXI, data products (version 7L) were downloaded from the website provided by RIKEN, JAXA and the MAXI team.[3] A total number of 31,927 observation intervals were obtained, covering the time period from 2009 August to 2020 June. The exposure time of each interval is ∼90 minutes.

3. Analysis

3.1. 35 Day States

In order to study the relation between the orbital cycles of the binary system and the super-orbital 35 day cycle, we define the 35 day phase, so that the orbital lightcurves during the different 35 day states can be distinguished from each other.

The time of the X-ray turn-on (TO) for 35 day cycles has been determined for more than 150 cycles over the last two decades (Leahy & Igna 2010; Leahy & Wang 2020). As a result, the 35 day phases can be determined with a high confidence level. We use the peak times of the Swift/BAT 35 day cycles in Table 1 of Leahy & Wang (2020) to calculate the 35 day phase values for both the Swift/BAT and MAXI observations.

The definition of the 35 day phase follows from Leahy & Wang (2020), where the peak of the MH state when the flux reaches its maximum is defined to be $\phi_{35\mathrm{day}} = 0.0$.[4] Under this definition, TO has a 35 day phase $\phi_{35\mathrm{day},TO} = 0.87$ (Table 2 of Leahy & Wang 2021). Here, the data is split into the following "states" of the 35 day cycle: mid MH $0.9 \leqslant \phi_{35\mathrm{day}} < 1.1$; decline of MH (DEC) $0.1 \leqslant \phi_{35\mathrm{day}} < 0.22$; first low state (LS1) $0.22 \leqslant \phi_{35\mathrm{day}} < 0.4$; SH $0.4 \leqslant \phi_{35\mathrm{day}} < 0.65$; second low state (LS2) $0.65 \leqslant \phi_{35\mathrm{day}} < 0.8$; and rise of MH or TO $0.8 \leqslant \phi_{35\mathrm{day}} < 0.9$.

To better compare between the three missions, we analyze the data with observation times that overlap with those of Swift/BAT, i.e., MJD53438-58692 (5255 days). As a result, the RXTE/ASM data cover MJD53438-55923 for 2486 days, and the MAXI data cover MJD55057-58692 for 3636 days. The total number of data points used for the study of orbital lightcurves is 69,806 for Swift/BAT, 34,958 for RXTE/ASM, and 29,061 for MAXI.

3.2. Time-average Orbital Lightcurves

We calculate the orbital phase from the observation time in MJD with Equation (5) of Staubert et al. (2009). The mideclipse of the neutron star Her X-1 by its companion Her HZ defines orbital phase zero. For the different 35 day states, orbital lightcurves were created for Swift/BAT, RXTE/ASM, and the three energy bands of MAXI.

The data were binned by orbital phase. The longest exposure time in the Swift/BAT data is 2672 (44.5 minutes), so we split the orbital lightcurves of Swift/BAT into 50 bins, such that each bin covers an orbital phase interval of 0.02, or ∼49 minutes. Because RXTE/ASM and MAXI have longer exposure times (∼90 minutes), we reduce the resolution of the orbital lightcurves to 25 bins. In each bin, if N points are covered, the averaged count rate is the mean value $R_{\mathrm{bin}} = \frac{1}{N}\sum_{i=0}^{N-1} R_i$, and the error is calculated as $\epsilon_{\mathrm{bin}} = \frac{1}{N}\sqrt{\sum_{i=0}^{N-1} \epsilon_i^2}$.

[1] https://swift.gsfc.nasa.gov/results/transients/
[2] http://xte.mit.edu/asmlc/ASM.html
[3] http://maxi.riken.jp/star_data/J1657+353/J1657+353.html
[4] Most earlier definitions of the 35 day phase zero are "start of TO," which is earlier by ∼0.13 in the 35 day phase than the definition used here.

Table 1
Average Numbers of Points in Each Bin for the Different 35 Day States

State	ϕ_{35day} Range	Swift/BAT	RXTE/ASM	MAXI
MH	$0.9 \sim 1.1$	272	282	242
DEC	$0.1 \sim 0.22$	165	173	157
LS1	$0.22 \sim 0.4$	257	260	207
SH	$0.4 \sim 0.65$	356	345	275
LS2	$0.65 \sim 0.8$	209	206	174
TO	$0.8 \sim 0.9$	138	132	108

Note. The ranges of the 35 day phases are left-inclusive.

A total of 2946 orbital cycles are found in the Swift/BAT data, 1286 in RXTE/ASM, and 1361 in MAXI. The average numbers of the points averaged in each bin of the different 35 day states are summarized in Table 1. The distribution of the data between the different states varies by a factor of ∼2–3.

We show the orbital lightcurves for the different 35 day states for Swift/BAT and the three bands of MAXI in Figure 1. The 2–12 keV lightcurves for RXTE/ASM are compared with those of MAXI in the Appendix (Figure A1).

3.3. Lightcurve Fits for Dips and Eclipses during MH and DEC

During MH and DEC, dips and eclipse egresses and ingresses are clearly seen. The orbital lightcurves during the MH state show small enough errors that we subdivide MH into smaller 35 day phase intervals. The MH is split into four equally spaced 35 day "substates": $0.9 \sim 0.95$, $0.95 \sim 1.0$, $0.0 \sim 0.05$, and $0.05 \sim 0.1$ (named MH-a, -b, -c, and -d, respectively). Table 2 gives the number of orbits of data included in each of the substates. We fit models to the lightcurves for the substates of MH and for DEC to measure the dips, ingresses, and egresses.

The eclipses during MH last from orbital phase 0.93 to 1.07 (Leahy & Yoshida 1995). Leahy & Igna (2011) found the distribution of dips with respect to orbital phase (their Figure B1). The fraction of time in the dips is at a minimum between orbital phase 0.2 and 0.4. Because the averaged lightcurves during MH (see Section 4 below) show a constant count rate in this range, we average over orbital phase 0.2–0.4 to determine a "no-dip" count rate for each energy band, labeled R_{max}.

3.3.1. Eclipse Egress

No dips are seen during orbital phase $0.0 \leqslant \phi_{orb} < 0.4$, so we can fit eclipse egresses independently of dips and ingresses. During egress, the companion HZ Her moves away from the line of sight to Her X-1, and results in an increase in count rate.

We first fit the egress with a linear function (joined to a 0 count rate during eclipse). The linear function results in poor fits. We find that egress can be satisfactorily fit with two linear functions:

$$y_{eg} = \begin{cases} 0 & x < \phi_1 \\ y_{eg1} = k_1 x + b_1 & \phi_1 \leqslant x < \phi_2 \\ y_{eg2} = k_2 x + b_2 & \phi_2 \leqslant x < \phi_3 \\ R_{max} & x \geqslant \phi_3 \end{cases}. \quad (1)$$

The count rate starts to rise from zero at orbital phase ϕ_1, which defines the start of the first linear function y_{eg1}. The two linear functions are joined at (ϕ_2, $R_{ratio}R_{max}$). The "no-dip" rate R_{max} is reached at orbital phase ϕ_3, which defines the end of y_{eg2}. As a result, $k_1 = \frac{R_{ratio} \times R_{max}}{\phi_2 - \phi_1}$, $b_1 = -k_1\phi_1$, and $k_2 = \frac{(1 - R_{ratio}) \times R_{max}}{\phi_3 - \phi_2}$, $b_2 = R_{max} - k_2\phi_3$.

By inspection of the lightcurves, we set $\phi_1 = 0.03$ for Swift/BAT, which has 0.02 width bins, and $\phi_1 = 0.0$ for RXTE/ASM and MAXI, which have 0.04 width bins. The three free parameters are fitted to the data: ϕ_2 (the orbital phase where the two linear functions join), ϕ_3 (the orbital phase where the count rate reaches R_{max}), and R_{ratio} (the ratio of the count rate to R_{max} at the join point).

3.3.2. Ingress and Pre-eclipse Dip

Because the dips can occur during orbital phase $0.4 \leqslant \phi_{orb} \leqslant 1.0$, some of the dips overlap ingresses. Thus, we fit ingresses and dips at the same time. We find satisfactory fits with a linear function for ingresses and a Gaussian for dips. We make a further assumption of the symmetrical eclipse, so that k, the absolute value of the slope, is the same as that for egresses when fitting ingresses with a single linear function.

The fit function for ingresses is:

$$y_{in} = \begin{cases} R_{max} & x \leqslant \phi_0 - \dfrac{R_{max}}{k} \\ y_{eg} = -k(x - \phi_0) & \phi_0 - \dfrac{R_{max}}{k} < x < \phi_0 \end{cases}; \quad (2)$$

and the fit function for dips is:

$$y_{dip} = A_{dip} \exp\left(\frac{(x - \mu)^2}{-2\sigma^2}\right). \quad (3)$$

Thus the fit function for orbital phase $0.4 \sim \phi_0$ includes both components:

$$y_{in,dip} = y_{in} \times (1 - y_{dip}). \quad (4)$$

The four free parameters are: $\phi_0 \in [0.91, 0.95]$; $A_{Dip} \in [0, 1]$; $\mu \in [0.7, 0.99]$; and $\sigma \in [0.02, 0.12]$.

3.3.3. Additional Dip at Orbital Phase ∼0.6 during MH-a

An additional dip is visible near orbital phase 0.6, prior to the pre-eclipse dip, for all energy bands during the MH-a ($0.90 \leqslant \phi_{35day} < 0.95$) substate. The same wide dip is visible during TO, but it is not seen in later MH substates or DEC. For MH-a, we fit a second Gaussian function between orbital phase 0.4 and 0.8:

$$y_{dip2} = A_{dip2} \exp\left(\frac{(x - \mu_2)^2}{-2\sigma_2^2}\right), \quad (5)$$

so that, for MH-a, the combined fit function is then:

$$y_{in,dip2} = y_{in,dip} \times (1 - y_{dip2}). \quad (6)$$

There are three additional parameters for the second dip: $A_{Dip2} \in [0, 1]$; $\mu_2 \in [0.4, 0.8]$; and $\sigma_2 \in [0, 0.4]$. We modify the lower limit of μ to be 0.85 and the upper limit of σ to be 0.05 in order to minimize the influence of the additional dip near orbital phase 0.6 on the fit of the pre-eclipse dip.

To find the 1σ error of the fit parameters, we calculate the χ^2 values for various parameter sets. The upper and lower limits of any specific parameter p are the maximum and minimum

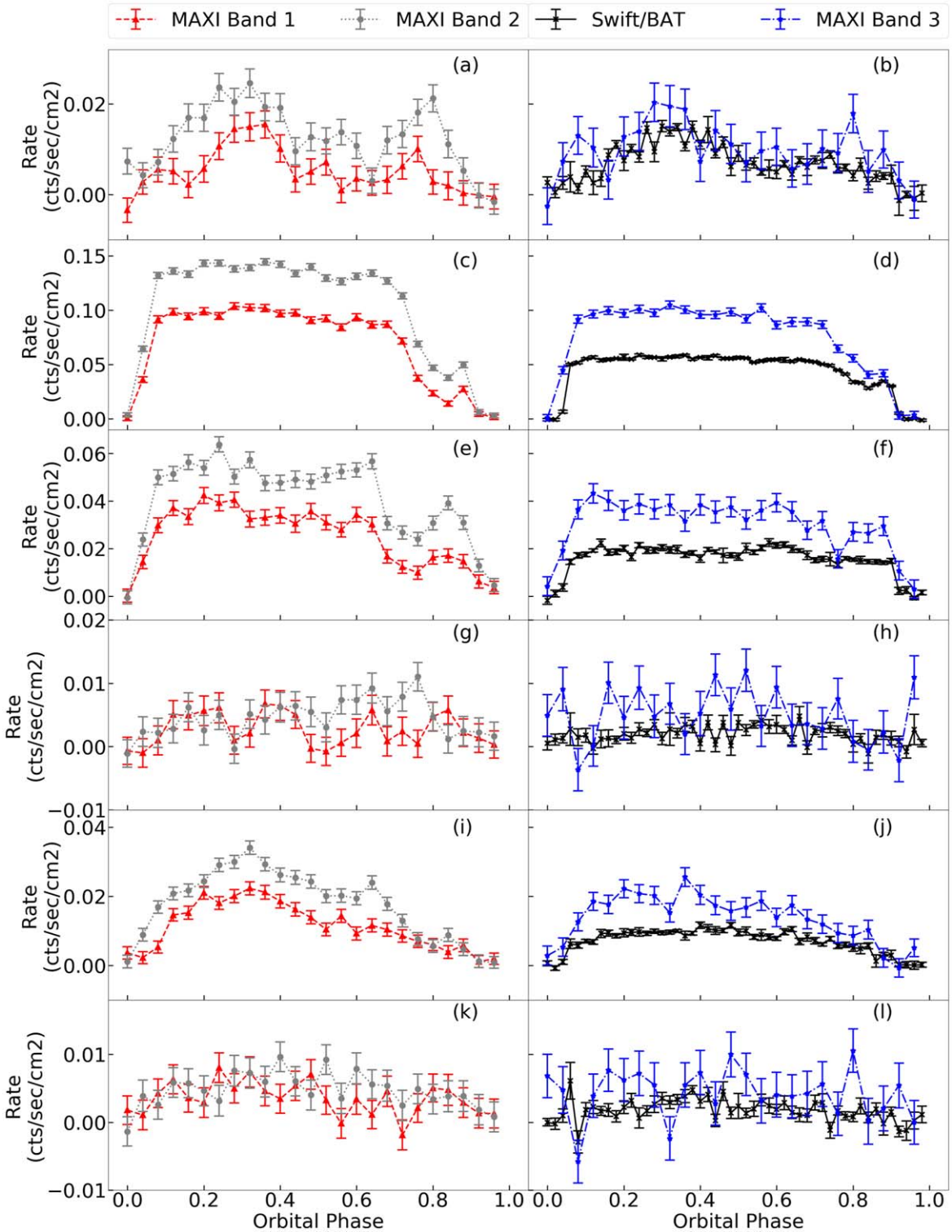

Figure 1. Orbital phase lightcurves of Swift/BAT (50 bins) and the three MAXI bands (25 bins) during all six 35 day states. (a) and (b): TO ($0.8 \leqslant \phi_{35\mathrm{day}} < 0.9$); (c) and (d): MH ($0.9 \leqslant \phi_{35\mathrm{day}} < 1.1$); (e) and (f): DEC ($0.1 \leqslant \phi_{35\mathrm{day}} < 0.22$); (g) and (h): LS1 ($0.22 \leqslant \phi_{35\mathrm{day}} < 0.4$); (i) and (j): SH ($0.4 \leqslant \phi_{35\mathrm{day}} < 0.65$); and (k) and (l): LS2 ($0.65 \leqslant \phi_{35\mathrm{day}} < 0.8$).

values of those with $\chi^2 \in [\chi^2_{\mathrm{min}},\ \chi^2_{\mathrm{min}} + \Delta\chi^2]$ (with the method and $\Delta\chi^2$ specified in Press et al. 2002).

3.4. Column Density and Transmission Fraction versus Orbital Phase

We quantitatively measure the effect of attenuating matter on the X-ray spectrum by fitting the count rates in different energy bands. This can be done for any orbital phase, thus determining the absorption versus orbital phase, and how it changes with the 35 day phase. This can be done for the MH substates and DEC, which have small enough errors.

The model assumption is that the observed count rate, compared to the unattenuated rate versus orbital phase, is a result of two factors. One factor is photoelectric absorption and

Table 2
Number of Orbits Averaged during MH Substates and DEC

# of Orbits	MH-a	MH-b	MH-c	MH-d	DEC
RXTE/ASM	64	64	63	62	163
MAXI	65	68	77	79	185
Swift/BAT	146	143	152	139	360

Note. For RXTE/ASM and MAXI, 35 day phases are only calculated for the time periods overlapping with Swift/BAT, resulting in a smaller number of orbits.

the second is energy-independent loss. The latter could be a blockage by optically thick matter or a scattering of flux out of the line of sight. The maximum rate is assumed to be the unattenuated rate from the central source. To reduce errors, the maximum $R_{\max}$ is taken as the mean value of the rates between orbital phases 0.2 and 0.4.

As a result, the observed count rate R can be expressed as:

$$\frac{R}{R_{\max}} = fe^{-\sigma_{\rm pe}(E)N_H}, \tag{7}$$

where $R_{\max}$ is the nonabsorbed count rate, $N_{\rm H}$ is the column density of the accretion stream, $\sigma_{\rm pe}$ is the photoelectric absorption cross section, and f is the transmission fraction caused by energy-independent loss.

The photoelectric absorption cross section is well known as a function of energy. We use WebPIMMS[5] to find the averaged photoelectric cross section for the X-ray energy band, including instrument response, for Swift/BAT and for MAXI Bands 1, 2, and 3. To do this calculation, we input the Her X-1 peak MH spectrum as the incident spectrum to convolve with the detectors' responses. The resulting effective cross sections are: MAXI Band 1 (2–4 keV) – $\sigma_{{\rm pe},M1} = 7.7 \times 10^{-24}\,{\rm cm}^2$; Band 2 (4–10 keV) - $\sigma_{{\rm pe},M2} = 9.8 \times 10^{-25}\,{\rm cm}^2$; Band 3 (10–20 keV) – $\sigma_{{\rm pe},M3} = 1.6 \times 10^{-25}\,{\rm cm}^2$; and Swift/BAT (15–50 keV) – $\sigma_{{\rm pe},B} = 3.5 \times 10^{-26}\,{\rm cm}^2$.

With these cross sections, we solve for the column density $N_{\rm H}$ and the transmission fraction f at any given orbital phase with the observed count rates from any two energy bands. Two independent calculations of $N_{\rm H}$ and f are carried out: one from MAXI Band 1 and Band 3, and the other from MAXI Band 1 and Swift/BAT. We find consistent results, with the latter giving smaller errors, so we show the results using MAXI Band 1 and Swift/BAT below.

4. Results

Figure 1 shows the orbital lightcurves for MH for the six different 35 day states (TO, MH, DEC, LS1, SH, and LS2) in the Swift/BAT and MAXI bands. For each 35 day state, the lightcurve shapes are similar across the energy bands. By summing the count rates of MAXI Band 1 and Band 2, we obtain MAXI 2–10 keV lightcurves to compare to those from RXTE/ASM (2–12 keV; Figure A1). The MAXI 2–10 keV and RXTE/ASM lightcurves have consistent shapes: the normalization is different because of different sensitivities, and RXTE/ASM has larger background subtraction errors.

[5] https://heasarc.gsfc.nasa.gov/cgi-bin/Tools/w3pimms/w3pimms_pro.pl

4.1. Low-state Lightcurves

To reduce the X-ray data error bars for LS1 and LS2, we summed the Swift/BAT and the three bands of MAXI lightcurves (Figure 2). The orbital lightcurves during the two low states exhibit little difference in shape, both showing a count rate of ∼4% of the MH out-of-eclipse value (a mean of $0.2 \leqslant \phi_{\rm orb} \leqslant 0.6$). The relative count rate of LS with respect to MH peak value is consistent through all five energy bands, as well as with other X-ray observations, e.g., BeppoSAX (Oosterbroek et al. 2000) and AstroSat/SXT (Leahy & Chen 2019). A χ^2 comparison test on the LS1 and LS2 lightcurves from Swift/BAT yields a χ^2 value of 28.1, which has a probability level of 0.26. To test if there is an intrinsic phase offset between LS1 and LS2, we shift LS2 with respect to LS1, and calculate χ^2. The minimum χ^2 is at zero bins offset (Figure 3), showing no detectable offset.

A χ^2 comparison test is performed on our X-ray orbital lightcurves for LS1 and LS2 with the optical ones from Jurua et al. (2011). To align their 35 day phase ranges with our two LS definitions, we average their lightcurves over the 35 day phases 0.35–0.50 for LS1 and 0.80–0.90 for LS2. The optical lightcurves are binned to 25 bins to match the X-ray lightcurve bins.

The χ^2 with no offset between X-ray and optical lightcurves is 58.9 for LS1 and 77.5 for LS2. However, we find a smaller χ^2 when a shift is included. The two lightcurves are best aligned when the optical is shifted one bin earlier than the X-ray (1.63 hr) for LS1, with $\chi^2_{\rm min} = 57.8$, and two bins earlier for LS2 (3.26 hr), with $\chi^2_{\rm min} = 70.6$ (see the bottom panel of Figure 3).

4.2. Short High Lightcurve

From the previous X-ray observations, e.g., the 35 day lightcurves from RXTE/PCA by Leahy & Igna (2011), a typical peak rate of SH is about 25% of MH. A similar value is seen in the 35 day lightcurves derived from the long-term analysis of Swift/BAT, e.g., the bottom panel of Figure 2 in Leahy & Wang (2020). If we compare the SH peak count rate from our lightcurves (in all bands) to that of the mean of MH and DEC, we find 29%, which is comparable to previous studies.

In all energy bands, the SH lightcurve (Figure 1, panels (i) and (j)) is asymmetric about orbital phase 0.5. The decrease starts slightly before $\phi_{\rm orb} \sim 0.4$, when HZ Her is behind Her X-1 and the accretion disk. In addition, this asymmetry is stronger in the lower energy bands (MAXI Band 1 and Band 2), and weakest at the higher energy band of Swift/BAT, which is least affected by absorption. Thus, the decrease is likely due to absorption. This confirms the results from the study by Leahy & Igna (2011), which find SH to be dominated by absorption dips after orbital phase ∼0.4.

4.3. Main High Lightcurves

The MH lightcurves in different energy bands are shown in Figure 1 (panels (c) and (d)). The previous analysis to obtain a time-averaged MH orbital lightcurve was done using ASM data (Scott & Leahy 1999, their Figure 4). Our ASM MH lightcurve is shown in Figure A1 (panel (b)). It is consistent with the previous one, including the small rise at orbital phase 0.85 just before ingress. Ours has smaller errors: the previous one was constructed using ∼850 days of data from MJD50146 to

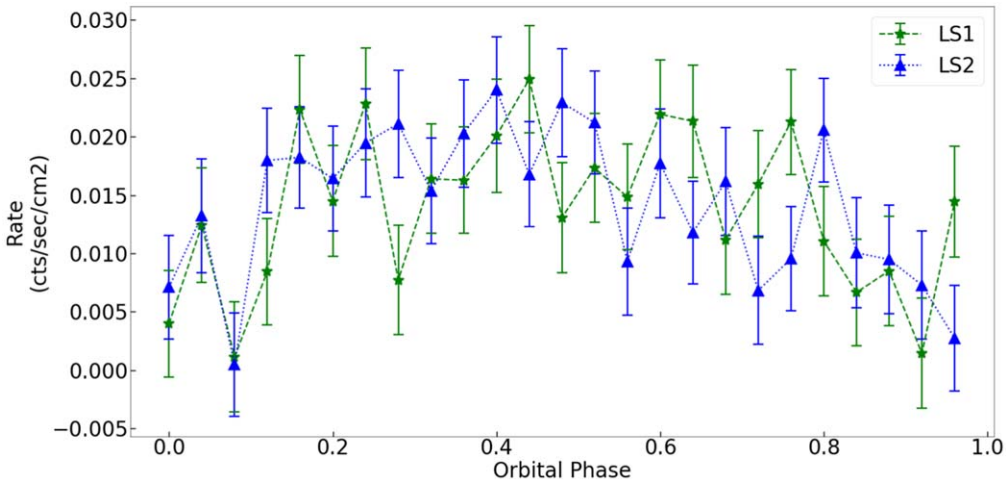

Figure 2. The summed orbital lightcurves during LS1 ($0.22 \leqslant \phi_{35\mathrm{day}} < 0.4$) and LS2 ($0.65 \leqslant \phi_{35\mathrm{day}} < 0.8$) from MAXI Bands 1, 2, and 3 and Swift/BAT.

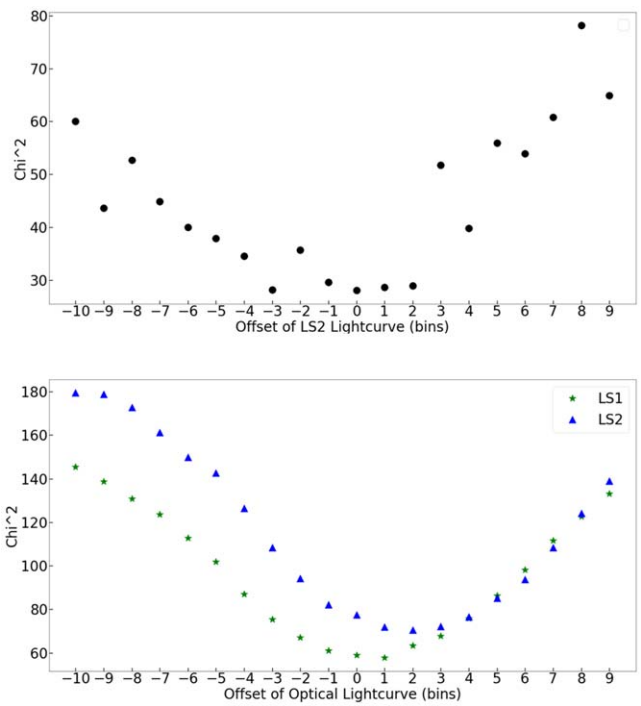

Figure 3. χ^2 vs. offset for LS1 and LS2. Top panel: comparison of the LS1 and LS2 orbital lightcurves from Swift/BAT. A negative number of bins means an offset of LS2 to a later orbital phase than LS1. Bottom panel: comparison of the LS1 and LS2 optical lightcurves (Jurua et al. 2011) with the sum of the Swift/BAT and the three bands of MAXI lightcurves for LS1 and LS2. The minimum χ^2 occurs when the optical is shifted one bin earlier for LS1 (0.04 in orbital phase, or 1.63 hr) and two bins earlier for LS2 (0.08 in orbital phase, or 3.26 hr).

50912, whereas ours is constructed using ∼3250 days of data from MJD53438 to 55923.

Using the four substates (MH-a, -b, -c, and -d) and DEC, we examine the dependence of the lightcurves on the 35 day phases.

4.3.1. Dip Parameters' Dependence on 35 Day Phase

The left column of Figure 4 shows the orbital lightcurves with the best-fit egress–dip–ingress functions for the Swift/BAT data. The fits for RXTE/ASM and for the three MAXI bands give very similar results, and are included in Appendix B. There is an additional dip near orbital phase 0.6, preceding the pre-eclipse dip during MH-a. This dip will be discussed in Section 4.3.2.

The parameters of best fit are listed as tables in Appendix C, along with the χ^2 values. Errors are calculated as described in Section 3.3.2. In Figure 5, we plot μ, σ, and A_{dip} versus orbital phase. In addition, the softness ratio (SR) between MAXI Band 1 (2–4 keV; R_1) and Swift/BAT (15–50 keV; R_2) is plotted in panel (d) of Figure 5 for the MH substates and for DEC. The drop in SR indicates photoelectric absorption, where soft X-rays are more strongly reduced than hard X-rays.

The best-fit functions for the MH substate lightcurves are shown as the solid lines in the left column of Figure 4, with the best-fit parameters and their errors shown in panels (a), (b), and (c) of Figure 5. For all energy bands, the pre-eclipse dip phase shifts to earlier orbital phases (μ decreases; panel (a)) and becomes shallower (A_{dip} decreases; panel (c)).

As energy increases (from Band 1 to Band 2 to Band 3 to Swift/BAT), there is marginal evidence that the dips occur later in orbital phase (panel (a)). There is stronger evidence that the dip depth decreases with energy (panel (c)), as would be expected if the dips are mainly caused by absorption. No significant evidence is found that the width of the dip depends on the 35 day phase or energy (panel (b)). The mean value of the dip width is $\sigma_{\mathrm{mean}} = 0.07208$, or 2.9 hr, and the standard deviation is 0.02203 (0.90 hr). This gives the FWHM of the pre-eclipse dip in the orbital phase as $2\sqrt{2\ln 2}\ \sigma_{\mathrm{mean}} = 0.1697$ (6.9 hr), comparable to the duration of the eclipse.

4.3.2. Parameters for the Dip at Orbital Phase 0.6 during MH-a

During the MH-a state, there is an additional absorption dip around orbital phase 0.6. The Gaussian fit shows that the depth decreases as energy increases, indicating an absorption process, while the position and width of the dip in the orbital phase are consistent among different energy bands.

This wide absorption dip during early MH is much shallower than the pre-eclipse dip, and it is not symmetrical in the orbital phase. As an alternative approach, we approximate its depth by manually selecting a middle point where the count rate is R_{dip} and compare it to R_{max}. The percentage depth of the dip is then defined as: $\%Depth = 1 - \frac{R_{\mathrm{dip}}}{R_{\mathrm{max}}}$. Table 3 lists the middle points chosen and the corresponding percentage depths for all five energy bands, which are consistent with the results from the best Gaussian fits. MAXI and RXTE/ASM agree with each other, with a depth of

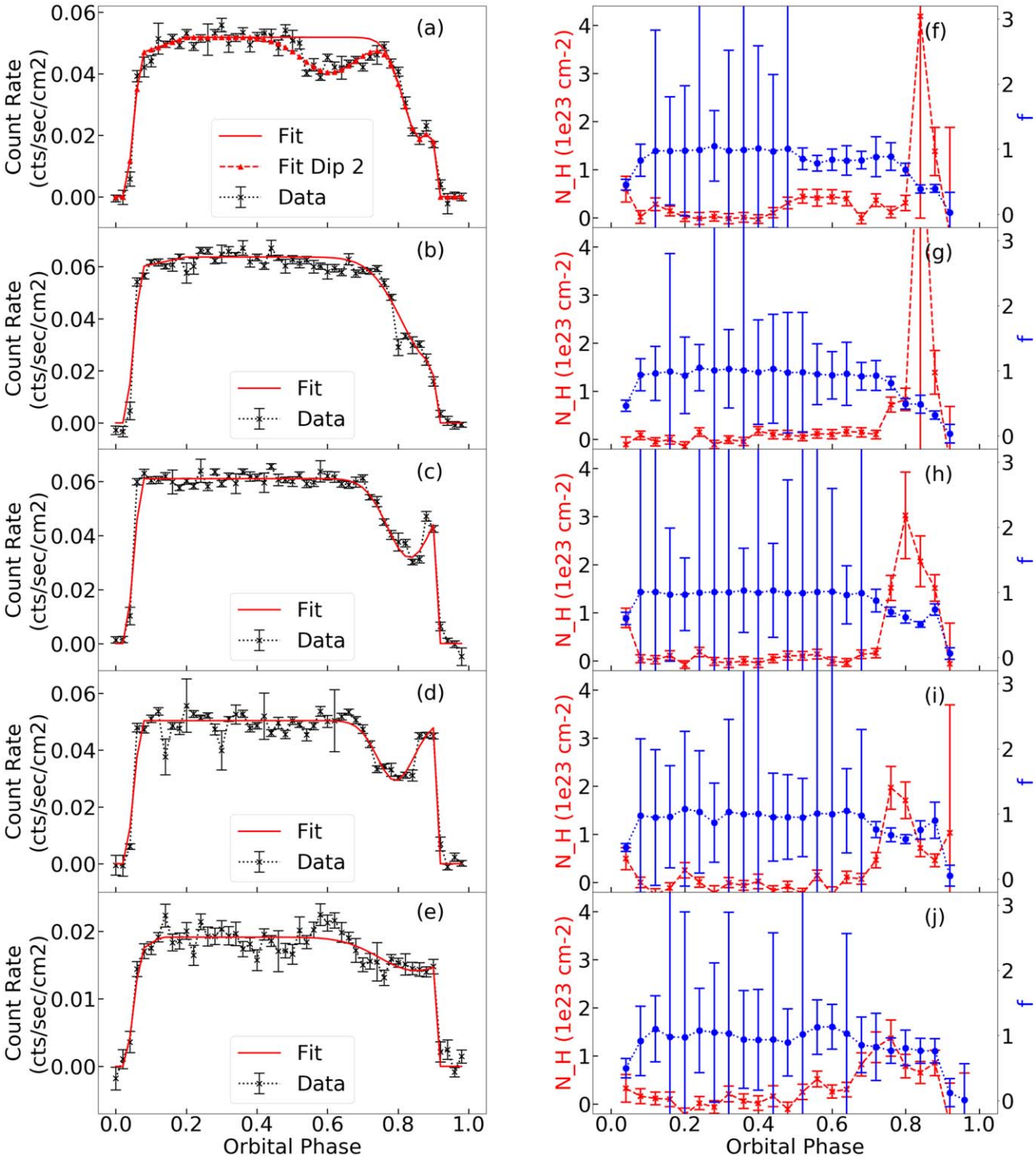

Figure 4. Left column: the best fits of orbital phase lightcurves from Swift/BAT during MH and DEC (50 bins). See Appendix B for the plots of MAXI Bands 1, 2, and 3 and of RXTE/ASM. Right column: the column density $N_{\rm H}$ (red crosses) and the transmission fraction f (blue dots) calculated from MAXI Band 1 (2–4 keV) and Swift/BAT (15–50 keV). From top to bottom: (a) and (f) MH-a ($0.9 \leqslant \phi_{35\rm day} < 0.95$); (b) and (g) MH-b ($0.95 \leqslant \phi_{35\rm day} < 1.0$); (c) and (h) MH-c ($0.0 \leqslant \phi_{35\rm day} < 0.05$); (d) and (i) MH-d ($0.05 \leqslant \phi_{35\rm day} < 0.1$); and (e) and (j) DEC ($0.1 \leqslant \phi_{35\rm day} < 0.22$).

30%–40% of the averaged maximum count rate. Swift/BAT gives a much lower value of 18%. This means there is combined absorption and energy-independent blockage during the dip.

The orbital phase when this wide dip appears does not show strong dependence on energy in our analysis because of two major limitations in data. Although long-term observations provide full coverage of the data in orbital lightcurves, the variation among the individual cycles is lost in the process, and a longer exposure time restricts the resolution in orbital phase. In addition, large errors (see Figure 1) during the 35 day states, other than MH, make it not possible to identify the wide dip during TO and even earlier 35 day phases.

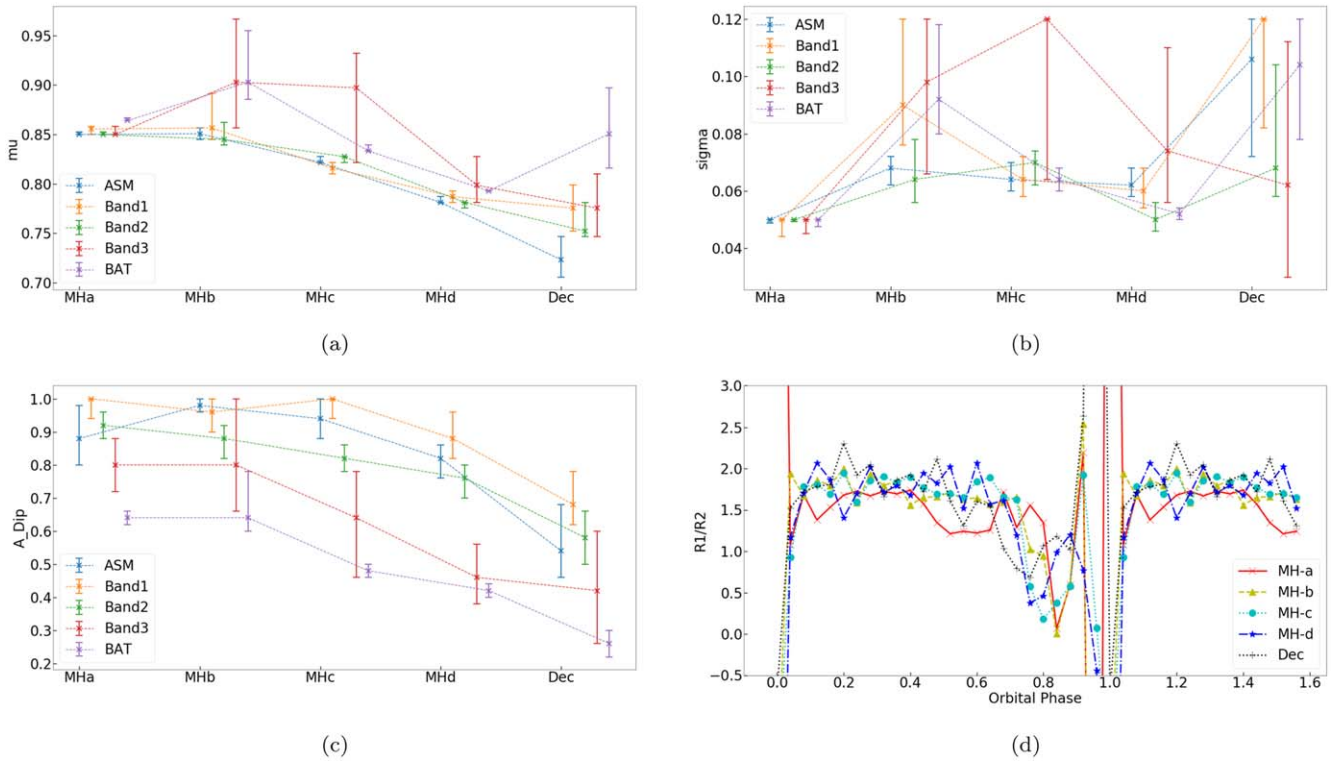

Figure 5. The fit parameters of the orbital lightcurves during MH. (a) Center of dip (μ); (b) width of dip (σ); (c) depth of dip ($A_{\rm dip}$); and (d) the softness ratio (R_1/R_2) of 1.5 orbits for the MH substates and DEC, where R_1 = MAXI Band 1 (2–4 keV) and R_2 = Swift/BAT (15–50 keV). The errors of SR are $\simeq \pm 0.2$, except during eclipse, for which they increase to $\sim$2 and higher.

Table 3
Approximated Percentage Depths and Best Gaussian Fit Parameters of the Absorption Dip at $\phi_{\rm orb} \sim 0.6$

	$\phi_{\rm dip}$	% Depth	$A_{\rm dip2}$	μ_2	σ_2
RXTE/ASM	0.56	39.53%	0.45	0.60	0.08
MAXI Band 1	0.56	39.45%	0.40	0.60	0.10
MAXI Band 2	0.56	35.42%	0.30	0.58	0.10
MAXI Band 3	0.64	31.94%	0.30	0.62	0.08
Swift/BAT	0.62	17.58%	0.20	0.60	0.08

4.4. Column Density and Transmission Fraction versus Orbital Phase

We show results for $N_{\rm H}$ and f determined from MAXI Band 1 and Swift/BAT in Figure 4 (right column). Despite the large errors, the transmission fraction is consistent with unity for orbital phases between 0.1 and 0.6–0.8, depending on the 35 day phase. The column density is small, except during dips. During the pre-eclipse dip, we see a clear rise in the column density to a few times $10^{23}\,{\rm cm}^{-2}$, and a drop in the transmission fraction f. This can be explained by increased absorption in the system, which is accompanied by energy-independent losses.

The out-of-dip column density, except near eclipse, where the count rates are too low to measure $N_{\rm H}$ and f, is $\sim 10^{21}\,{\rm cm}^{-2}$. During MH-a, the maximum column density of the extra absorption dip is $4.5 \times 10^{22}\,{\rm cm}^{-2}$ at orbital phase 0.52. After the MH peak, the maximum column density of the pre-eclipse dip drops from $3.0 \times 10^{23}\,{\rm cm}^{-2}$ at orbital phase 0.8 during MH-c to $1.4 \times 10^{23}\,{\rm cm}^{-2}$ at orbital phase 0.76 in DEC.

5. Discussion

5.1. Low States

We find an orbital phase delay of the optical lightcurves during LS1 and LS2 compared to the X-ray lightcurves of LS1 and LS2. An X-ray–optical offset has not been reported before, and is possibly due to the different disk shadow affecting the illumination region on HZ Her.

Despite the limitations of the different methods, there is consistency in shape between our orbital lightcurve and those measured in previous X-ray studies. Thus, the LS orbital lightcurves are stable over time periods of $\sim$30 yr.

Limited by the sensitivity resolution of the data, we do not clearly see eclipses in our LS lightcurves, unlike some other studies. E.g., Abdallah & Leahy (2015) used RXTE/PCA data and clearly see eclipses, finding that the LS X-ray emission is mainly from the reflection off the face of HZ Her and from the accretion disk corona (their Figure 5). More recently, Shakura et al. (2021) studied two observation periods during LS of Her X-1/HZ Her from the SRG/eROSITA all-sky survey (0.2–8 keV). They proposed a similar model of LS X-ray emission, but further break the reflection component from the companion star into an optically thick cold atmosphere and an optically thin hot corona above.

5.2. Short High State

In SH, the observer views the inner rings of the disk, and the system emits soft X-rays ($\sim$1 keV), mainly from the inner disk (McCray et al. 1982; Leahy 2002). Harder X-rays ($>$1 keV, which we measure) are mainly from scattering by the inner disk and material above the disk, while the central neutron star

source of the X-rays is obscured by the inner disk edge (Scott et al. 2000; Leahy 2002).

The decrease of X-ray emission for SH starts at orbital phase 0.35 (Figure 1), thus it cannot be caused by the accretion disk, which rotates with a 35 day period. The companion is not in the observer's line of sight over the full orbital phase interval of 0.07–0.93. However, the accretion stream leads the companion in its orbit (see Figure 1 of Igna & Leahy 2012), and the accretion stream–disk interaction site was proposed by that work as the cause of dips, including the 35 day and orbital phase dependence of the dips.

A detailed picture of the orbital lightcurve during SH was given by Abdallah & Leahy (2015), with four successive orbits of high-sensitivity RXTE/PCA data (their Figure 1). The first orbit of SH has a delayed increase of X-ray flux versus orbital phase, but the remaining three orbits have an early increase. This implies that the average orbital lightcurve over the full SH state is a combination of different shapes. This is further verified by the amalgamation of SH orbital lightcurves presented by Leahy & Igna (2011, their Figure 6), which show a wide range of count rates during SH. The average count rate for SH from RXTE/PCA in that work is consistent with that determined here from the Swift/BAT, MAXI, and ASM data.

5.3. Main High State

The 35 day phase-averaged (phase 0.9–1.1) orbital lightcurve is shown in Figure 1 (panels (c) and (d)). It is consistent with previously measured MH orbital lightcurves (Scott & Leahy 1999; Leahy & Igna 2011), but here is measured in several energy bands. We used the multiband lightcurves, subdivided into substates of MH, to derive the absorption column density, $N_{\rm H}$, and the transmission fraction, f, versus orbital phase (Figure 4, right column).

The main results from the current measurement of $N_{\rm H}$ and f are: (i) the $N_{\rm H}$ of the time-average orbital lightcurve changes systematically with the 35 day phase; and (ii) the f is consistent with 1 for the orbital phases that are not affected by egress, dip, or ingress. $N_{\rm H}$ versus orbital phase throughout MH is measured here for the first time. f has been measured previously for short intervals of time using X-ray spectra, and is measured here for the first time for all of MH. We find that $N_{\rm H}$ increases are invariably accompanied by f decreases. This shows that dips are accompanied by significant decreases in energy-independent transmission, i.e., there is optically thick matter in addition to cold matter absorption associated with the dips.

The $N_{\rm H}$ and f measurements and the lightcurve fits (shown in Figure 4) both show the marching of the dips to earlier orbital phases as the 35 day phase increases. Thus, we have measured clearly the marching of the dips in fine (0.05) 35 day phase intervals. This verifies the previous measurement of the orbital phases of individual dips versus the 35 day phase (Figure 9 of Leahy & Igna 2011). The dip marching can be explained by the accretion stream–disk impact model (Igna & Leahy 2012, see their Figure 6). It can also be explained by the dips model of Shakura et al. (1999), which involves an out-of-plane stream caused by the asymmetric illumination of HZ Her by X-rays shadowed by the precessing accretion disk.

The orbital phase distribution of the dips during MH was measured from RXTE/PCA observations by Leahy & Igna (2011, their Figure 5). That work showed that the dips are not uniformly spaced in orbital phase, but cluster mainly after orbital phase 0.7, with a second smaller cluster near phase 0.55 (see their Figure B1). This is consistent with what we find (Figure 4, both columns), but the current work shows, for the first time, the evolution of the dip properties with the 35 day phase.

Observations with higher time resolution and sensitivity were analyzed by previous studies to see the details and variability of individual dips. E.g., Igna & Leahy (2011) analyzed RXTE/PCA data and gave three types of pre-eclipse dips with a variety of time durations. I.e., individual dips are often only minutes in duration, and their occurrence is scattered in orbital phase (Leahy & Igna 2011), so that the long-term time-average dips that we measure are a combination of dip and no-dip data. Thus, our measured width is wider than that for individual dips, and the measured $N_{\rm H}$ and f are lower and higher, respectively, than those for individual dips. The advantage of the current analysis is that it gives the systematic (time-average) behavior of the dips.

Previous studies found the column density during the pre-eclipse dip to be on the order of $10^{24}\,{\rm cm}^{-2}$ (Reynolds & Parmar 1995; Stelzer et al. 1999; İnam & Baykal 2005). The column density we derived is lower by a factor of ten. This is not too surprising, because individual dips vary in duration and orbital phase, and the averaging of dozens of dips yields a smaller $N_{\rm H}$.

When comparing the pre-eclipse dips with the anomalous dips statistically, we find the maximum column density to be about 6.7 times higher in pre-eclipse dips near the MH peak. During DEC, the value drops to 3.1, but the pre-eclipse dips still have a higher maximum column density. In comparison, Reynolds & Parmar (1995) found the factor to be 2.5 times higher for column density during the pre-eclipse dips. We confirm their result of weaker anomalous dips. It is reasonable to see a larger factor between the two types of dips from our analysis, as pre-eclipse dips are less scattered and produce higher maxima when averaged. Anomalous dips are in general shorter in duration as well (Reynolds & Parmar 1995).

In spite of the limitations of our long-term observations, previous references support our conclusion of the clustering of absorption dips. Individual pieces of observations, such as the two anomalous dips observed by EXOSAT in 1984 and 1985 (Reynolds & Parmar 1995), are indeed observed near orbital phase 0.6 within the 35 day phase range of MH-a, among many others. A statistical study of RXTE/ASM data (Scott & Leahy 1999) indicates regular absorption dips between orbital phase 0.4 and 0.6 during MH (see their Figure 5), where several anomalous dips can be seen. Leahy & Igna (2011) find longer in-dip times in this orbital phase range for both MH and SH. In particular, their Figure 9 indicates a dip at TO from orbital phase 0.3–0.7, which is not seen during most of MH. Panels (a) and (b) in our Figure 1 produce the same result.

5.4. Other Remarks

Eclipse egress and ingress are studied at higher time resolution and sensitivity in previous studies (e.g., Leahy 1995; Leahy & Yoshida 1995; Leahy & Abdallah 2014; Leahy 2015), and those are better suited to measuring eclipse properties. Here, we included egress and ingress in our lightcurve model in order to extract the properties of the dips, so there are no new results on egress and ingress in this paper.

Early studies on the 35 day cycle of Her X-1 often found the TO to cluster near orbital phases 0.2 and 0.7 (Scott & Leahy 1999), which has been rejected by more recent observational studies (Leahy & Igna 2010; Leahy & Wang 2020). With the average orbital lightcurves we present, both can be logically explained. The tendency of 35 day TOs near orbital phase 0.7 is possibly due to the regular presence of pre-eclipse dips during early MH and TO, when the observed rate increases after dip. In contrast, TOs near orbital phase 0.2 are more likely to be seen when eclipse egress reveals the neutron star to the observer.

A recent model for dips was proposed by Igna & Leahy (2012). The model gives good predictions on the marching of pre-eclipse dips, as well as the width in orbital phase. However, the model predicts a dip marching from orbital phase 1.0–0.85 as the 35 day phase increases from MH-a, which does not align with the observations and occurs late by 0.15 in orbital phase. This can be seen by comparing their model 35 day phase versus orbital plot (Figure 6 of Igna & Leahy 2012) with the dips data plot (Figure 9 of Leahy & Igna 2011): the observed dips are shifted earlier (to the lower left). We have carried out test calculations that indicate that the disagreement cannot be resolved by simple changes to the disk shape. Thus, we suggest a different shape of accretion stream than used by Igna & Leahy (2012) (more curved) or the out-of-plane stream model of Shakura et al. (1999). One of these models is likely to be better at matching the observed orbital phase versus 35 day phase diagram for dips.

We plan to carry out such a detailed dips model study in future.

6. Summary and Conclusion

In this paper, we analyze broadband X-ray observations from the binary system Her X-1/HZ Her with MAXI (2–20 keV; three bands) and Swift/BAT (15–50 keV) data. We subdivide the super-orbital 35 day cycle of Her X-1/HZ Her into six states and present long-term average orbital lightcurves in multiple energy bands of X-rays. We present the most complete set of orbital lightcurves of Her X-1 in several X-ray bands, and the change in these lightcurves with 35 day phase (Figure 1 here). These lightcurves will serve as valuable inputs for modeling the accretion disk structure, which is the cause of the lightcurve changes as the disk rotates with its 35 day period.

The orbital lightcurves during LS1 and LS2 are consistent with each other in X-rays. We newly report an offset of the optical lightcurve later than X-ray by a few hours during LS. The orbital lightcurves during SH are asymmetric with binary orbit, which is explained by the time averaging of rapidly varying lightcurves. The MH lightcurves have the best signal-to-noise, so we further divide them into four substates.

Pre-eclipse dips are studied during the MH substates and DEC. We confirm many previously known results (e.g., summarized in Leahy & Igna 2011). The marching of pre-eclipse dips toward earlier 35 day phases is confirmed. We find the dips to be shallower in later 35 day phases and in higher energy bands. Anomalous dips are found to cluster near orbital phase 0.6 during early MH. We confirm that anomalous dips are distinct from and weaker than the pre-eclipse dips. The new result is the systematic change in average dip properties with the 35 day phase, as summarized in Figure 4 above.

This research is supported by a grant from the Natural Sciences and Engineering Research Council of Canada. This research has made use of the MAXI data provided by RIKEN, JAXA and the MAXI team.

Appendix A
Orbital Lightcurves of RXTE/ASM and MAXI

Figure A1 shows the orbital lightcurves derived from the RXTE/ASM data for the six states of the 35 day cycle. For comparison, we show the MAXI 2–20 keV and MAXI 2–10 keV lightcurves on the same plot.

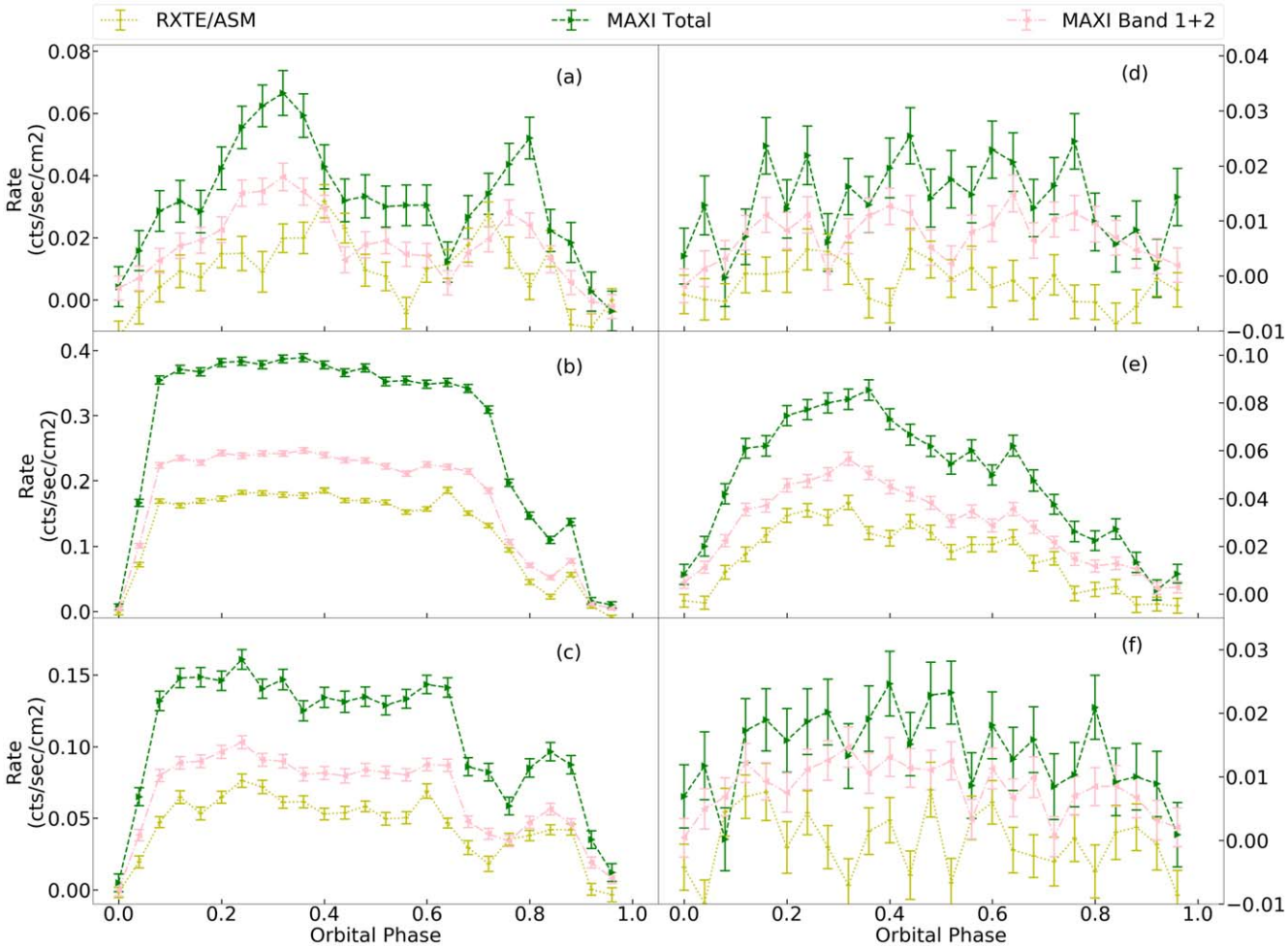

Figure A1. Orbital phase lightcurves (25 bins) of RXTE/ASM (2–12 keV), MAXI Total (2–20 keV), and Bands 1 + 2 (2–10 keV) during all six 35 day states: (a) TO ($0.8 \leqslant \phi_{35\mathrm{day}} < 0.9$); (b) MH ($0.9 \leqslant \phi_{35\mathrm{day}} < 1.1$); (c) DEC ($0.1 \leqslant \phi_{35\mathrm{day}} < 0.22$); (d) LS1 ($0.22 \leqslant \phi_{35\mathrm{day}} < 0.4$); (e) SH ($0.4 \leqslant \phi_{35\mathrm{day}} < 0.65$); and (f) LS2 ($0.65 \leqslant \phi_{35\mathrm{day}} < 0.8$). The left *y*-axis scale is for the panels in the left column, and the right *y*-axis scale is for the right panels.

Appendix B
Orbital Lightcurve Fits during MH and DEC for RXTE/ASM and MAXI

The lightcurve model fits, described in Section 3.3 above, are shown for the MAXI Band 1, Band 2, and Band 3 lightcurves and the RXTE/ASM lightcurves in Figure B1.

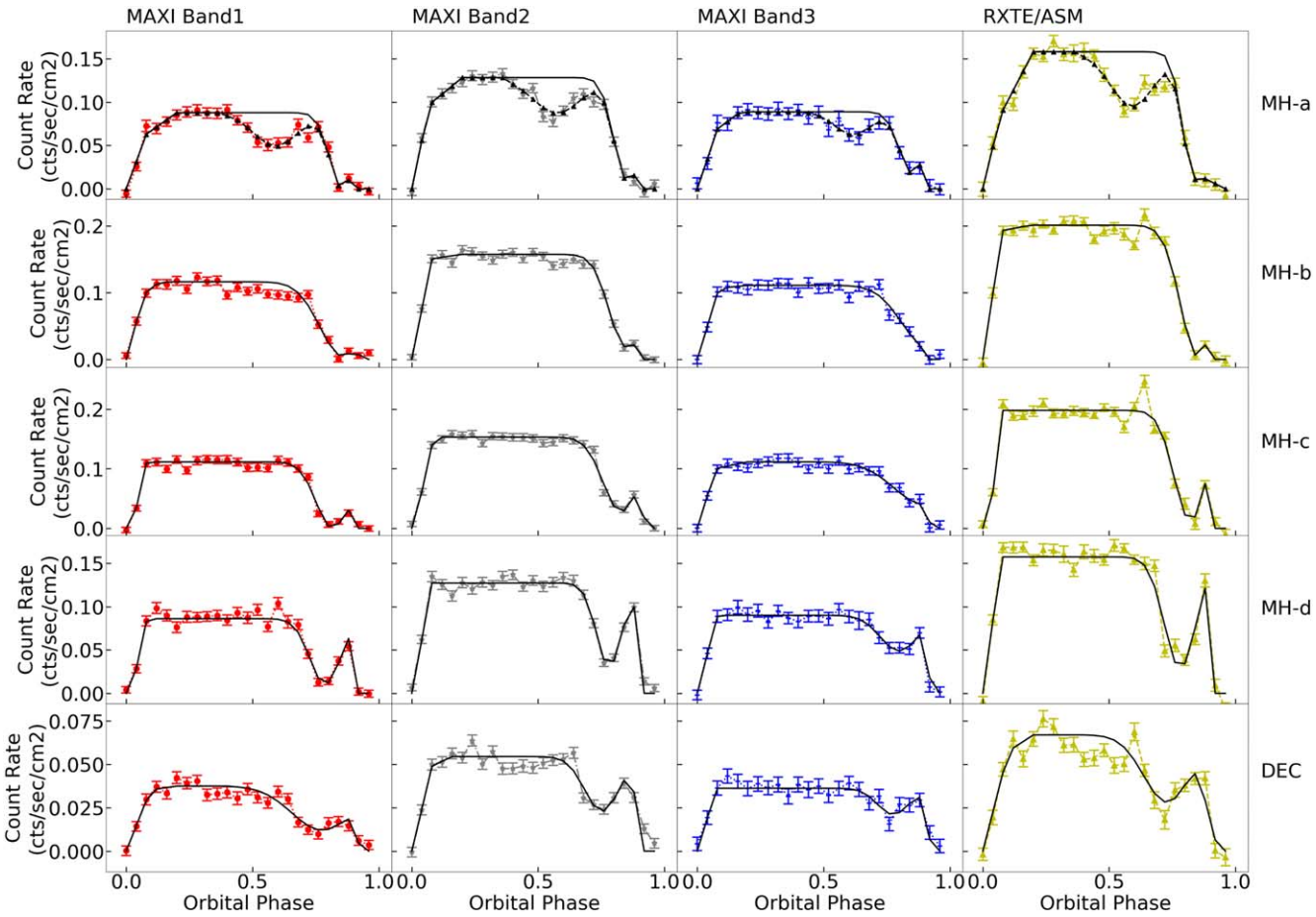

Figure B1. The best fits of the averaged orbital lightcurves during MH substates and DEC for MAXI Band 1 (2–4 keV), Band 2 (4–10 keV), Band 3 (10–20 keV), and RXTE/ASM (12–20 keV). 35 day states: MH-a ($0.9 \leqslant \phi_{35\mathrm{day}} < 0.95$), MH-b ($0.95 \leqslant \phi_{35\mathrm{day}} < 1.0$), MH-c ($0.0 \leqslant \phi_{35\mathrm{day}} < 0.05$), MH-d ($0.05 \leqslant \phi_{35\mathrm{day}} < 0.1$), and DEC ($0.1 \leqslant \phi_{35\mathrm{day}} < 0.22$). The lightcurves are plotted on the same scale for each state.

Appendix C
Best-fit Parameters of Orbital Lightcurves during MH

As the χ^2 values of the best-fit functions in Table 4 show, introducing a second Gaussian dip greatly improves the fit of the orbital lightcurves during MH-a. The rest of the 35 day substates are fit well without a second dip.

Table 5 gives the best-fit parameters and their 1σ uncertainties for the lightcurve fits for the five substates and five energy bands.

Table 4
χ^2 Values of the Best-fit Functions during MH Substates and DEC

	RXTE /ASM	MAXI Band 1	MAXI Band 2	MAXI Band 3	Swift /BAT
MH-a (2 dips)	37.882	25.541	30.985	11.202	133.220
MH-a	397.674	202.014	253.042	51.706	632.858
MH-b	49.609	67.078	29.729	21.430	202.647
MH-c	66.583	32.544	35.817	20.989	302.852
MH-d	84.018	30.968	36.111	12.493	247.258
DEC	90.376	32.305	71.286	17.701	76.304

Note. RXTE/ASM and MAXI orbital lightcurves have 25 bins, while Swift/BAT has 50 bins.

Table 5
The Five Substates: Best-fit Parameters (value) and 1σ Uncertainties (unc.)

parameter	MH-a value	unc.	MH-b value	unc.	MH-c value	unc.	MH-d value	unc.	DEC value	unc.
$A_{\rm Dip}$										
RXTE/ASM	0.880	−0.080	0.980	−0.020	0.940	−0.060	0.820	−0.060	0.540	−0.080
		+0.100		+0.020		+0.060		+0.040		+0.140
MAXI/Band1	1.000	−0.060	0.960	−0.060	1.000	−0.060	0.880	−0.060	0.680	−0.060
		+0.000		+0.040		+0.000		+0.080		+0.100
MAXI/Band2	0.920	−0.040	0.880	−0.060	0.820	−0.040	0.760	−0.060	0.580	−0.080
		+0.040		+0.040		+0.040		+0.040		+0.080
MAXI/Band3	0.800	−0.080	0.800	−0.140	0.640	−0.180	0.460	−0.080	0.420	−0.160
		+0.080		+0.200		+0.140		+0.100		+0.180
Swift/BAT	0.640	−0.020	0.640	−0.040	0.480	−0.020	0.420	−0.020	0.260	−0.040
		+0.020		+0.140		+0.020		+0.020		+0.040
μ										
RXTE/ASM	0.850	−0.000	0.851	−0.006	0.822	−0.000	0.781	−0.000	0.723	−0.017
		+0.003		+0.006		+0.006		+0.006		+0.023
MAXI/Band1	0.856	−0.006	0.857	−0.012	0.816	−0.006	0.787	−0.006	0.775	−0.023
		+0.003		+0.035		+0.006		+0.006		+0.023
MAXI/Band2	0.850	−0.000	0.845	−0.006	0.828	−0.006	0.781	−0.006	0.752	−0.006
		+0.003		+0.017		+0.000		+0.000		+0.029
MAXI/Band3	0.850	−0.000	0.903	−0.046	0.897	−0.075	0.799	−0.017	0.775	−0.029
		+0.008		+0.064		+0.035		+0.029		+0.035
Swift/BAT	0.864	−0.000	0.903	−0.017	0.833	−0.000	0.793	−0.000	0.851	−0.035
		+0.003		+0.052		+0.006		+0.000		+0.046
σ										
RXTE/ASM	0.050	−0.001	0.068	−0.006	0.064	−0.004	0.062	−0.004	0.106	−0.034
		+0.000		+0.004		+0.006		+0.006		+0.014
MAXI/Band1	0.050	−0.006	0.090	−0.014	0.064	−0.006	0.060	−0.006	0.120	−0.038
		+0.000		+0.030		+0.008		+0.008		+0.000
MAXI/Band2	0.050	−0.001	0.064	−0.008	0.070	−0.008	0.050	−0.004	0.068	−0.010
		+0.000		+0.014		+0.004		+0.006		+0.036
MAXI/Band3	0.050	−0.005	0.098	−0.032	0.120	−0.056	0.074	−0.018	0.062	−0.032
		+0.000		+0.022		+0.000		+0.036		+0.050
Swift/BAT	0.050	−0.002	0.092	−0.012	0.064	−0.004	0.052	−0.002	0.104	−0.026

Table 5
(Continued)

parameter	MH-a value	unc.	MH-b value	unc.	MH-c value	unc.	MH-d value	unc.	DEC value	unc.
		+0.000		+0.026		+0.004		+0.002		+0.016
ϕ_0										
RXTE/ASM	0.930	−0.000	0.910	−0.000	0.910	−0.000	0.910	−0.000	0.930	−0.000
		+0.000		+0.000		+0.000		+0.000		+0.020
MAXI/Band1	0.910	−0.000	0.930	−0.020	0.910	−0.000	0.910	−0.000	0.930	−0.020
		+0.000		+0.020		+0.000		+0.000		+0.000
MAXI/Band2	0.910	−0.000	0.910	−0.000	0.930	−0.000	0.910	−0.000	0.910	−0.000
		+0.000		+0.020		+0.000		+0.000		+0.020
MAXI/Band3	0.910	−0.000	0.910	−0.000	0.930	−0.020	0.930	−0.000	0.930	−0.000
		+0.000		+0.040		+0.000		+0.000		+0.020
Swift/BAT	0.910	−0.000	0.910	−0.000	0.910	−0.000	0.910	−0.000	0.910	−0.000
		+0.000		+0.000		+0.000		+0.000		+0.000
ϕ_2										
RXTE/ASM	0.070	−0.000	0.078	−0.008	0.078	−0.008	0.070	−0.000	0.101	−0.031
		+0.031		+0.010		+0.000		+0.013		+0.034
MAXI/Band1	0.080	−0.010	0.070	−0.000	0.070	−0.000	0.078	−0.008	0.096	−0.026
		+0.034		+0.034		+0.008		+0.021		+0.036
MAXI/Band2	0.070	−0.000	0.080	−0.010	0.075	−0.005	0.075	−0.005	0.080	−0.010
		+0.023		+0.010		+0.023		+0.010		+0.021
MAXI/Band3	0.080	−0.010	0.086	−0.016	0.073	−0.003	0.075	−0.005	0.073	−0.003
		+0.060		+0.021		+0.031		+0.021		+0.034
Swift/BAT	0.070	−0.000	0.070	−0.000	0.070	−0.000	0.070	−0.000	0.070	−0.000
		+0.003		+0.000		+0.000		+0.000		+0.008
ϕ_3										
RXTE/ASM	0.200	−0.024	0.188	−0.118	0.078	−0.008	0.078	−0.008	0.200	−0.120
		+0.000		+0.012		+0.003		+0.122		+0.000
MAXI/Band1	0.200	−0.066	0.132	−0.062	0.080	−0.010	0.080	−0.010	0.200	−0.130
		+0.000		+0.068		+0.005		+0.120		+0.000
MAXI/Band2	0.200	−0.055	0.200	−0.130	0.083	−0.013	0.078	−0.008	0.159	−0.089
		+0.000		+0.000		+0.117		+0.122		+0.041
MAXI/Band3	0.171	−0.101	0.200	−0.130	0.200	−0.130	0.083	−0.013	0.078	−0.008
		+0.029		+0.000		+0.000		+0.117		+0.122
Swift/BAT	0.200	−0.062	0.200	−0.052	0.200	−0.130	0.200	−0.130	0.127	−0.057
		+0.000		+0.000		+0.000		+0.000		+0.073
$R_{\rm ratio}$										
RXTE/ASM	0.540	−0.080	0.960	−0.240	0.600	−0.200	0.940	−0.160	0.860	−0.580
		+0.160		+0.040		+0.160		+0.060		+0.140
MAXI/Band1	0.720	−0.160	0.840	−0.200	0.540	−0.220	0.640	−0.320	0.940	−0.600
		+0.220		+0.160		+0.280		+0.360		+0.060
MAXI/Band2	0.760	−0.080	0.960	−0.260	0.760	−0.220	0.920	−0.240	0.900	−0.360
		+0.140		+0.040		+0.240		+0.080		+0.100
MAXI/Band3	0.780	−0.500	0.960	−0.480	0.900	−0.340	0.960	−0.380	0.960	−0.540
		+0.220		+0.040		+0.100		+0.040		+0.040
Swift/BAT	0.900	−0.100	0.940	−0.020	1.000	−0.000	1.000	−0.060	0.900	−0.120
		+0.040		+0.020		+0.000		+0.000		+0.100

ORCID iDs

Yuyang Wang https://orcid.org/0000-0002-4228-2478
Denis Leahy https://orcid.org/0000-0002-4814-958X

References

İnam, S. C., & Baykal, A. 2005, MNRAS, 361, 1393
Abdallah, M. H., & Leahy, D. A. 2015, MNRAS, 453, 4222
Deeter, J., Crosa, L., Gerend, D., & Boynton, P. E. 1976, ApJ, 206, 861
Gerend, D., & Boynton, P. E. 1976, ApJ, 209, 562
Giacconi, R., Gursky, H., Kellogg, E., et al. 1973, ApJ, 184, 227
Gorecki, A., Levine, A., Bautz, M., et al. 1982, ApJ, 256, 234
Igna, C. D., & Leahy, D. A. 2011, MNRAS, 418, 2283
Igna, C. D., & Leahy, D. A. 2012, MNRAS, 425, 8
Jurua, E., Charles, P. A., Still, M., & Meintjes, P. J. 2011, MNRAS, 418, 437
Kolesnikov, D. A., Shakura, N. I., Postnov, K. A., et al. 2020, MNRAS, 499, 1747
Krimm, H. A., Holland, S. T., Corbet, R. H. D., et al. 2013, ApJS, 209, 14
Leahy, D., & Wang, Y. 2020, ApJ, 902, 146
Leahy, D., & Wang, Y. 2021, Univ, 7, 160
Leahy, D. A. 1995, ApJ, 450, 339
Leahy, D. A. 1997, MNRAS, 287, 622
Leahy, D. A. 2002, MNRAS, 334, 847
Leahy, D. A. 2003, MNRAS, 342, 446
Leahy, D. A. 2004, ApJ, 613, 517
Leahy, D. A. 2015, ApJ, 800, 32
Leahy, D. A., & Abdallah, M. H. 2014, ApJ, 793, 79
Leahy, D. A., & Chen, Y. 2019, ApJ, 871, 152
Leahy, D. A., & Igna, C. 2011, ApJ, 736, 74
Leahy, D. A., & Igna, C. D. 2010, ApJ, 713, 318
Leahy, D. A., Marshall, H., & Scott, D. M. 2000, ApJ, 542, 446
Leahy, D. A., Postma, J., & Chen, Y. 2020, ApJ, 889, 131
Leahy, D. A., & Yoshida, A. 1995, MNRAS, 276, 607
Levine, A. M., Bradt, H., Cui, W., et al. 1996, ApJL, 469, L33
Matsuoka, M., Kawasaki, K., Ueno, S., et al. 2009, PASJ, 61, 999
McCray, R. A., Shull, J. M., Boynton, P. E., et al. 1982, ApJ, 262, 301
Oegelman, H., & Truemper, J. 1988, MmSAI, 59, 169
Oosterbroek, T., Parmar, A. N., Dal Fiume, D., et al. 2000, A&A, 353, 575
Petterson, J. A. 1975, ApJL, 201, L61
Postnov, K., Shakura, N., Staubert, R., et al. 2013, MNRAS, 435, 1147
Press, W. H., Teukolsky, S. A., Vetterling, W. T., & Flannery, B. P. 2002, Numerical Recipes in C++ : The Art of Scientific Computing (Cambridge: Cambridge Univ. Press)
Reynolds, A. P., & Parmar, A. N. 1995, A&A, 297, 747
Scott, D. M., & Leahy, D. A. 1999, ApJ, 510, 974
Scott, D. M., Leahy, D. A., & Wilson, R. B. 2000, ApJ, 539, 392
Shakura, N. I., Kolesnikov, D. A., Medvedev, P. S., et al. 2021, A&A, 648, A39
Shakura, N. I., Prokhorov, M. E., Postnov, K. A., & Ketsaris, N. A. 1999, A&A, 348, 917
Staubert, R., Klochkov, D., & Wilms, J. 2009, A&A, 500, 883
Stelzer, B., Wilms, J., Staubert, R., Gruber, D., & Rothschild, R. 1999, A&A, 342, 736